Chinese Chemical Letters 33 (2022) 3955–3960

Contents lists available at ScienceDirect

Chinese Chemical Letters

journal homepage: www.elsevier.com/locate/cclet

A bi-component polyoxometalate-derivative cathode material showed impressive electrochemical performance for the aqueous zinc-ion batteries

Rui Huang[a,b], Weiwei Wang[a,c], Chi Zhang[a,b], Peng He[a,c], Yuyang Han[a,d], Nuo Chen[e], Jun Yan[a,b,c,d,*]

[a] College of Chemistry and Chemical Engineering, Central South University, Changsha 410083, China
[b] Hunan Provincial Key Laboratory of Chemical Power Sources, Central South University, Changsha 410083, China
[c] Hunan Provincial Key Laboratory of Efficient and Clean Utilization of Manganese Resources, Central South University, Changsha 410083, China
[d] Hunan Provincial Key Laboratory of Micro & Nano Materials Interface Science, Central South University, Changsha 410083, China
[e] Changsha Changjun High School, Changsha 410002, China

ARTICLE INFO

Article history:
Received 23 August 2021
Revised 9 October 2021
Accepted 30 November 2021
Available online 6 December 2021

Keywords:
Cathode material
Aqueous Zn-ion battery
Bi-component material
Polyoxometalate-derivative
Cathodic activation

ABSTRACT

Rechargeable aqueous zinc-ion batteries are recently gaining incremental attention because of low cost and material abundance, but their development is plagued by limited choices of cathode materials with satisfactory cycling performance. The polyoxometalates perform formidable redox stability and able to participate in multi-electron transfer, which was well-suited for energy storage. Herein, a bi-component polyoxometalate-derivative KNiVO ($K_2[Ni(H_2O)_6]_2[V_{10}O_{28}]\cdot 4H_2O$ polyoxometalates after annealing) is firstly demonstrated as a cathode material for aqueous ZIBs. The layered KV_3O_8 (KVO) In the bi-component material constitutes Zn^{2+} migration and storage channels (K^+ were substantially replaced by Zn^{2+} in the activation phase), and the three-dimensional NiV_3O_8 (NiVO) part acts as skeleton to stabilize the ion channels, which assist the cell to demonstrate a high-rate capacity and specific energy of 229.4 mAh/g and satisfactory cyclability (capacity retention of 99.1% after 4500 cycles at a current density of 4 A/g). These results prove the feasibility of POM as cathode materials precursor and put forward a novel pattern of the Zn^{2+} storage mechanism in the activated-KNiVO clusters, which also provide a new route for selecting or designing high-performance cathode for aqueous ZIBs and other advanced battery systems.

Nowadays, commercial nonaqueous lithium-ion batteries have occupied the main market of secondary battery in the energy storage field account of their high energy densities [1,2]. However, with the development of science and technology, human beings are paying attention to the use of energy resources (safe, efficient, clean and renewable) [3]. As available alternative, aqueous batteries based on K^+, Na^+, Ca^{2+}, Mg^{2+}, Al^{3+} and Zn^{2+} ions have aroused considerable interest owing to the lower price and higher security in contrast to LIBs [4–6]. Among them, rechargeable aqueous zinc-ion batteries (ZIBs) have fascinated increasing attention, which have a high theoretical specific gravimetric and volumetric capacities of 820 mAh/g, low redox potential of Zn^{2+}/Zn (−0.76 V *vs.* SHE), small ionic diameter (~0.43 nm for $Zn(H_2O)_6{}^{2+}$), as well as environmentally friendly [7]. Nevertheless, exploring suitable cathode materials with satisfactory cycling performance is still a tremendous challenge [8,9]. At present, most developed cathode materials are concentrated on vanadium oxides and manganese oxides [10–16]. Generally, there are two main strategies to improve the electrochemical properties of vanadium oxides materials, which are additional components doping or morphology tuning. For example, Al-Doped $V_{10}O_{24}\cdot 12H_2O$ with urchin-like morphology was reported as a long-life cathode material for ZIBs by Li *et al.* [17] Similarly, Islam and He reported that K^+ and Na^+ were intercalated V_2O_5 nanorods to improve specific capacity and cycle stability of ZIBs [18,19]. Chen and Qin reported monoclinic VO_2 hollow nanospheres and V_2O_5 hollow spheres as high rate cathode for aqueous ZIBs, while V_2O_5 nanosheets in-situ spaced with acetylene black was reported as a high-performance cathodes [20–25]. The application of manganese oxides as aqueous ZIBs cathode mainly focus on doping modification and electrically conductive coating (*e.g.*, carbon-encapsulated and polypyrrole-encapsulated)

---

[*] Corresponding author.
E-mail address: yanjun@csu.edu.cn (J. Yan).

https://doi.org/10.1016/j.cclet.2021.11.094
1001-8417/

[26–28]. In addition, cathode targeted at organics and new type of materials were reported as choice for aqueous zinc-ion batteries [29–31]. These methods are conducive to enlarge layer spacing and improve electrical conductivity for cathode materials [32,33]. However, as the morphology and composition of doping component varies widely, and it is still challenge to reliable doping and determine the function of all components in the cathode material developing [34,35].

Polyoxometalates (POMs) are anionic molecular metal oxides based on high-valent early transition metals (*e.g.*, Mo, W, V), holding a special position between monomeric oxometallate units and infinite metal oxide frameworks [36]. They exhibit unique structural and compositional properties, which lead to potential applications in various areas such as catalysis, energy conversion, molecular electronics and nano-carbon materials [37,38]. As an important and remarkable subclass, vanadium POMs can perform strong redox stability and able to participate in multi-electron transfer because the transition metals possess flexible oxidation states between +3 to +5, which were proven to be well-suited in the energy storage [39–42]. But it is also noticed that POMs are very fragile and their 3-D structure are easily destroyed during the galvanostatic discharge/charge process in lithium-ion and sodium-ion battery studies, which severely limited the application of POMs as energy storage materials [43–46]. For solving this contest, there are many classic types of POMs were modified (carbon material, conductive polymers, *etc.*) as anode materials to enhance electrical conductivity and stability [47–50]. Nevertheless, there are only a few researches applying POMs as aqueous ZIBs cathodes, for it is more difficult to insert Zn^{2+} into the cathode material due to its larger atomic mass and charge number than those of Li^{+}, and the structure of POMs was more easily dissolved in the aqueous electrolyte, which cause the unavailability of most methods applied in LIBs. Thus, larger multidimensional interconnected Zn^{2+} storage and migration channels and insoluble state of POMs-based material are two major concerns in the new ZIBs cathodes material design.

Herein, by annealing the single crystals of an ionic classic POM compound $K_2[Ni(H_2O)_6]_2[V_{10}O_{28}]\cdot4H_2O$, a bi-component polyoxometalate-derivative was prepared to exploit aqueous ZIBs with eminent discharge/charge properties. Through electrochemical and material characterization studies, the relationships between electrochemical properties (capacity, rate capability and cycling stability) and structural characteristics were proved. In the galvanostatic discharge/charge experiment, it can be found that the cell was activated during the first part of cycle, and the material became a porous and multi-dimensional interconnected skeleton structure, which was more stable and performed a better Zn^{2+} storage ability and ultrafast kinetics for ion insertion/extraction. As expected, the aqueous ZIBs demonstrate a better cycle stability (99.1% capacity retention after 4500 cycles) and specific capacity (229.4 mAh/g at current densities of 4 A/g). This conclusion not only presents prospects of POMs applied to the aqueous ZIBs field, but also displays a great potential of POMs in other energy batteries field.

The $K_2[Ni(H_2O)_6]_2[V_{10}O_{28}]\cdot4H_2O$ was synthesized through the water bath and oil bath methods. Typically, equal mass (0.5 g) of nickel (II) acetate tetrahydrate ($C_4H_6NiO_4\cdot4H_2O$) and potassium metavanadate (KVO_3) were dissolved in 100 ml deionized water at 80 °C for 30 min, then, the glacial acetic acid ($C_2H_4O_2$) was added to adjust pH until the solid was completely dissolved. The solution was condensed at 110 °C and the insoluble was filtered. Finally, the V_{10}-POM was crystallized at 30 °C. Yield: 84.2%. ICP-AES: (K:Ni:V = 1:1:5). TGA: 18% weight loss. Crystal X-ray diffraction XRD & Powder X-ray diffraction XRD: The actual value was matched well with theoretical value. CCDC: 2,099,784. Besides, the cathode material was obtained after annealing the POMs precursor in air atmosphere at 400 °C for 2 h.

The composite electrodes were prepared by mixing the KNiVO with super P and carboxymethyl cellulose (CMC) binder in the weight ratio 7:2:1 in deionized water to form a homogeneous slurry. This mixture was coated on a stainless-steel filter mesh (SSM, 304) using a doctor blade, the coating was dried in air at 60 °C. And the coating was punched into pieces with a diameter of 12 mm. These electrodes were then assembled in electrochemical cell with circular metallic zinc pieces with a diameter of 16 mm as the anode, and 7 mol/L solution of Zn_2SO_4 as electrolyte (20.13 g zinc sulfate heptahydrate was dissolved in 10 mL deionized water at 70 °C). Cyclic voltammetry and impedance were measured on Bipotentiostat (CS2350H), and galvanostatic discharge/charge data were recorded on the Land Battery Test System (CT2001A) instrument between 0.2 V and 1.8 V.

Crystal X-ray diffraction XRD data were collected on Bruker smart Apex 2. Powder X-ray diffraction XRD data were obtained with Rigaku MiniFlex 600-c. Scanning electron microscopy (SEM) images were obtained on JEOL-JSM7500F. Transmission electron microscope (TEM) images were photographed on FEI Tecnai F20, TF30. Raman spectra were acquired on Renishaw invia. X-ray photoelectron spectroscopy (XPS) were measured on Thermo Scientific K-Alpha^{+}. Inductively Coupled Plasma-Atomic Emission Spectrometry (ICP-AES) data were received by PerkinElmer 8300. Thermogravimetry (TG) data was obtained on STA 2500.

The classic precursor polyoxometalate $[V_{10}O_{28}]^{4-}$ was synthesised by using a classic "one-pot" method, and Ni ions were added to tune the microenvironment of POM cluster. Therefore, the ionic compound $K_2[Ni(H_2O)_6]_2[V_{10}O_{28}]\cdot4H_2O$ (V_{10}-POM) was obtained as high quality single crystals (Fig. 1a). TGA of the POM shows a weight loss starting at 40 °C and continues until 260 °C (Fig. S1 in Supporting information), indicating the presence of 16 molecules of coordinated water per crystal unit. Then, typical powder X- ray diffraction patterns and crystal X-ray diffraction data of V_{10}-POM are illustrated in Fig. S2 (Supporting information), and this crystal is identified to be pure phase by the perfect coincidence of the diffraction peaks. In order to solve the defect that POMs are easily dissolved in the aqueous electrolyte, V_{10}-POM crystal was annealed at 400 °C for 2 h and an insoluble derivative material (KNiVO) was received, and Fig. 1b shows the XRD pattern of the obtained material. A part of diffraction peaks at 12.404°, 26.110°, 30.441° and 31.294° are indexed to the NiV_3O_8 phase (JCPDS card No. 22–0454), and another part of peaks at 9.233°, 25.742° and 27.857° are assigned to characteristic reflections of KV_3O_8 (JCPDS card No. 22–

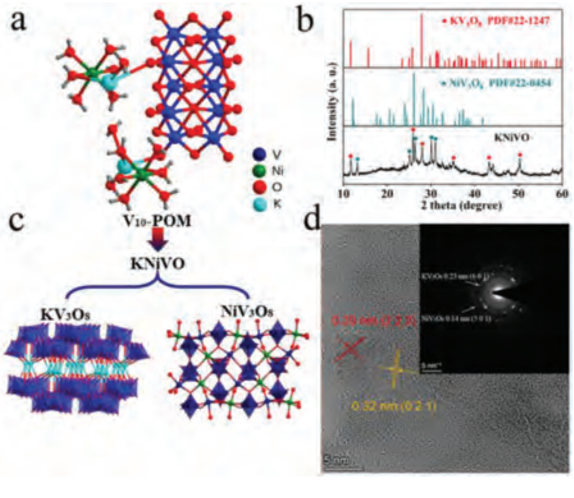

Fig. 1. (a) The molecular structure of the V_{10}-POM crystal. (b) XRD patterns of KNiVO material. (c) The structural change of V_{10}-POM crystal after annealing, and the components of KNiVO material. (d) HRTEM image and SAED pattern of inactivated KNiVO.

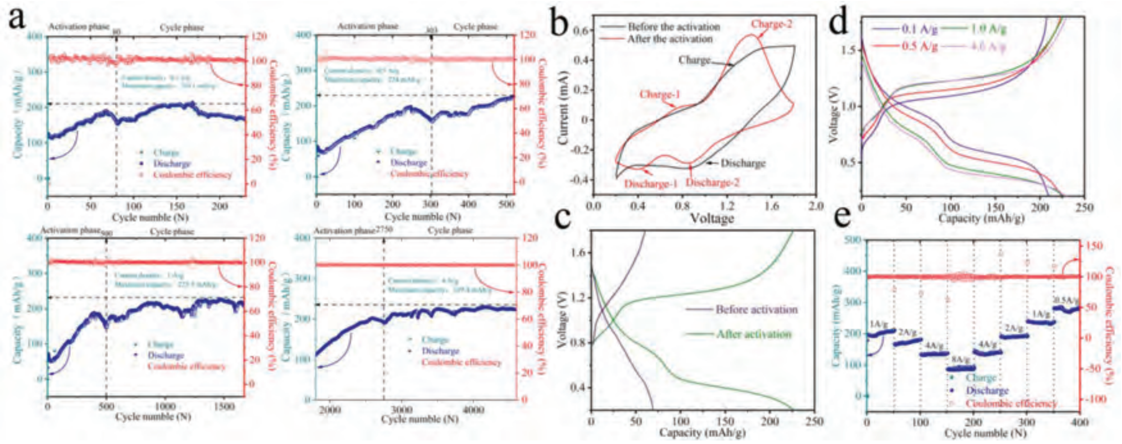

Fig. 2. (a) The capability of Zn/KNiVO battery at different current densities. (b,c) The cyclic voltammetry (CV) and galvanostatic charge-discharge (GCD) curves of the two before/after activated cycles. (d) The discharge/charge curves of the activated battery at different current densities. (e) The rate performance of the activated Zn/KNiVO battery.

1247). As shown in Fig. 1c, the anneal process changed the structure of vanadate in POM cluster. Besides, HR-TEM analysis shows that interplanar spacing of 0.29 and 0.32 nm corresponds to the (021) plane of NiV_3O_8 and the (222) plane of the KV_3O_8 (Fig. 1d), and the SAED pattern can also prove the composition of KNiVO. Meanwhile, XPS spectra date of KNiVO shows the valence state of Ni V K (Figs. S3-S5 in Supporting information). Partial of the $\{VO_6\}$ unit condensed to $\{VO_5\}$ fragment and formed a layered KV_3O_8 structure. Also, the further condensed $\{VO_4\}$ units were detected in block NiV_3O_8 phase. The ratio of KV_3O_8:NiV_3O_8 is about 2:3 based on the ICP results and extended annealing time does change the composite of the obtained materials.

To quest the application of KNiVO in aqueous ZIBs, the Zn/KNiVO cells were assembled with as-prepared cathode, the Zn foil as anode and 7 mol/L $ZnSO_4$ aqueous solution as electrolyte. Then, the capability was tested at different current densities from 0.1 A/g to 4 A/g, which was expressed in Fig. 2a. Obviously, the galvanostatic discharge/charge was divided into an activation phase and a cycle phase, and the activation speed was faster at a low current density since the ion exchange was more sufficient in the single-turn discharge/charge. And in the cycle phase, the cells displayed a superior cycle stability (capacity retention of 99.1% after 5000 cycles at current densities of 4 A/g) with an approximate specific capacity (the obtained discharge capacities were 210.1, 224, 225.5, 229.4 mAh/g at the current density of 0.1, 0.5, 1, 4 A/g). As expected, the CV curve of the Zn/KNiVO cell was changed dramatically after activation. Fig. 2b shows the CV curves of the two before/after activated cycles at the scan rate of 1 mV/s in the voltage window of 0.2–1.8 V. The obvious alteration between oxide peak in the range of 0.6–0.7 V and 1.2–1.6 V indicates the diversity of oxidation reactions and the formation of irreversible products in the charging process during the activation. This discovery can also be proved by the discrepancy of the discharge platform between 0.6–0.7 V and the charge platform between 1.2 V and 1.6 V in the galvanostatic charge-discharge curves (Fig. 2c) [51]. Besides, electrochemical impedance spectroscopy (EIS) measurements were carried out on the inactivated/activated Zn/KNiVO batteries to present the particularly reaction kinetics of the cathode materials. Generally, the semicircular intercept represents the interface membrane impedance (R_e), and the semicircular region represent the mixed impedance composed of interface membrane impedance and charge transfer impedance ($R_f//CPE_{sf}$, $R_{ct}//CPE_{sf}$). The slope of the line in the low-frequency region represents the Warburg impedance (Wo) formed by diffusion of ions inside the material [52]. The calculated R_e values of the two phases are very close, and the mixed impedance of KNiVO after activation is much lower than that inactivated, which proved a better contact between electrode/electrolyte interface in activated electrode (Fig. S6 in Supporting information). Fig. 2d shows the discharge/charge curves of the activated battery at different current densities. The charging platform is between 1 V and 1.4 V, and the discharging platform are consisted of the voltage range of 0.7–1.2 and 0.3–0.6 V. Simultaneously, rate performance of the activated cell was measured, which shows excellent rate capability (Fig. 2e). The cathode delivers reversible capacities of 285, 238, 191, 142, 92 mAh/g at current densities of 0.5, 1, 2, 4, 8 A/g, respectively. When the current density is switched back to 1 A/g from 8 A/g, the specific capacity returns to 242 mAh/g, implying the stability of the structure under a high-rate charge/discharge. Furthermore, the cathode material exhibits respectable cycling stability and the coulombic efficiency (CE) of nearly 100% were achieved after activation. Compared with the capacity reduction of existing cathode materials [11,12,18,22,53,54], KNiVO material shows better energy storage performance at high current density, which also exhibits an excellent cycling stability and longer cycle life after activation (Table 1).

Table 1
Electrochemical performance of cathode materials of AZIBs.

Cathode materials	Specific capacity, current density	Capacity retention (cycle number), current density	Ref.
KNiVO	229 mAh/g, 4 A/g	99.1% (4500), 4 A/g	This work
$H_2V_3O_8$	140 mAh/g, 5 A/g	94.3% (1000), 5 A/g	[11]
$K_2V_6O_{16}$	105 mAh/g, 3 A/g	61% (1000), 3 A/g	[12]
K-V_2O_5	155 mAh/g, 8 A/g	96% (1500), 8 A/g	[18]
V_2O_5 nanofibers	166 mAh/g, 2 C	81% (500), 2 C	[22]
V_2O_5 crystalline	113 mAh/g, 2 A/g	92% (400), 2 A/g	[53]
$(NH_4)_2V_{10}O_{25}$	123 mAh/g, 5 A/g	90.1% (5000), 5 A/g	[54]

To further explore the activation phenomenon and the electrochemical mechanism for Zn^{2+} migration in the cathode, and afford a good illustration to the diffusion-controlled and the pseudocapacitive-controlled capacities of the Zn/KNiVO battery [20,24,55], Fig. 3a displays a part voltammograms of the electrode after activation from 0.1 mV/s to 1.0 mV/s, which indicate an excellent reversibility. The degree of capacitive effect can be qualitatively analyzed according to the relationship between the measured current (i) and the scan rate (n) from the CV curves ($i = av^b$, where a and b are adjustable parameters, and the b value is between 0.5 and 1, $b = 0.5$ for a diffusion-controlled behavior and 1.0 for surface-controlled) [56]. Fig. 3b presents the plots of

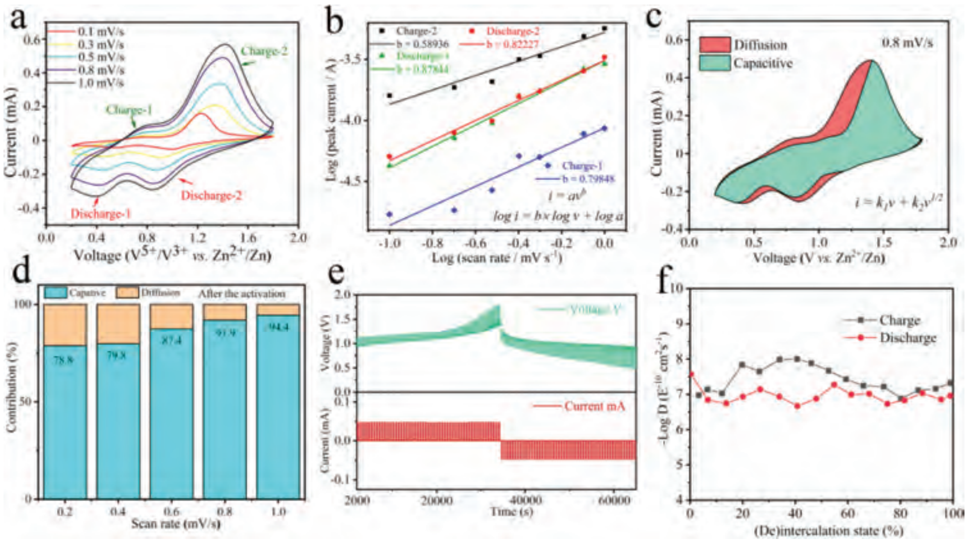

Fig. 3. (a) A part of CV curves of the activated KNiVO cathode at scan rates of 0.1–1.0 mV/s. (b) log(current) *vs.* log(scan rate) plots of four peaks in the CV curves during cycling. (c) Pseudocapacitive fraction (blue area) calculated at a scan rate of 0.8 mV/s. (d) Pseudocapacitive fractions at scan rates of 0.2, 0.4, 0.6, 0.8 and 1.0 mV/s. (e) A part of charge-discharge contours and time variation of GITT measurement. (f) Diffusivity coefficients of Zn^{2+} during the charging and discharging processes.

log(i) *versus* log(v) from 0.1 mV/s to 1 mV/s for both the cathodic and anodic peaks, and the b values at peaks of discharge and charge are 0.8784, 0.8227, 0.7985 and 0.5894, respectively, indicating a coordinated control process by pseudocapacitive and diffusion controlled in the activated cathode. Moreover, the proportion of the capacitance contribution was analyzed through the equation ($i = k_1 v + k_2 v^{1/2}$, the total current (i) is alienated to the capacitive contribution ($k_1 v$) and the diffusion-controlled current $k_2 v^{1/2}$) [57]. For example, Fig. 3c shows the capacitive contribution of 91.9% at a scan rate of 0.8 mV/s, and the capacitance contribution ratio of the activated KNiVO was always at a high level and gradually improved with the increasing scan rates (0.2–1.0 mV/s) at the same time (Fig. 3d). The large capacitive contribution proved that activated cathode deliver fast charge transfer kinetics. In addition, GITT was performed to explore the kinetics of Zn^{2+} diffusion (D_{Zn}) in the activated cathode. Fig. 3e shows a part of corresponding discharge curves (the complete curve was showed in Figs. S7 and S8 in Supporting information). And the D_{Zn} (Fig. 3f) for the activated-cathode can be calculated by the Ficks second law of diffusion (Fig. S9 in Supporting information) [21]. Surprisingly, the diffusion coefficient values are at the range of 10^{-6}–10^{-8} cm^2/s, which is obviously higher than those nanosheets of V_2O_5 (10^{-9} cm^2/s) [21] and other reported cathode materials such as the $NH_4V_4O_{10}$ (10^{-9}–10^{-8} cm^2/s) [14], La-Ca co-doped MnO (10^{-9}–10^{-8} cm^2/s) [27], layered $Ca_{0.28}MnO_2 \cdot 0.5H_2O$ (10^{-12}–10^{-10} cm^2/s) [31]. Obviously, the activated material can form more stable multidimensional interconnected Zn^{2+} migration and storage channels, which performed impressive diffusion capability. In the meantime, the origin KNiVO cathode was characterized in the same way (Figs. S10-S15 in Supporting information). It is worth noting that the material before activation has only three charge-discharge peaks and b values are 0.571, 0.579 and 0.639, which indicate the inactivated cathode was under the diffusion-controlled. Furthermore, the rate of capacitance contribution for origin cathode were significantly less than the activated cathode at the low scan rate. These results well prove that the activated cathode material has good reaction kinetics and exhibit excellent Zn^{2+} ions transfer and storage capacity.

In order to clarify the changes of KNiVO material during the activation process, the cathodes were characterized at different cycle stages. Judging from the matched well with the $Zn_4SO_4(OH)_6 \cdot 5H_2O$ (JCPDS card No. 39–0688), and another part of diffraction peaks at 12.292°, 30.1°, 34.192° and 36.462° are indexed to the XRD pattern of inactivated/activated KNiVO (Fig. S16 in Supporting information), the peaks for KV_3O_8 at the position at 9.233°, 25.742° and 27.857° disappeared but the characteristic peaks of NiV_3O_8 at 26.110° always exist. Moreover, the peak at 8.068° was $Zn_3(OH)_2V_2O_7 \cdot 2H_2O$ phase (#JCPDS card No. 50–0570). The XRD results can well elucidate the activation phenomenon and structure change during insertion/extraction of Zn^{2+} ions in the cathode. Firstly, Zn^{2+} embedded in KV_3O_8 layered channels and a part of K^+ were replaced irreversibly in the activation phase, which result in the disappearance of the KV_3O_8 peaks. In addition, the NiV_3O_8 clusters act as the reliable supporting structure to help the ions channels perform faster kinetics of Zn^{2+} insertion/extraction. Moreover, during the discharging process after activation, the stored Zn^{2+} was reduced to Zn-KNiVO and the V^{5+} (VO_4^{3-}) was reduced to V^{3+} ($V_2O_7^{8-}$), whereafter the intercalated Zn^{2+} was combined with $V_2O_7^{8-}$ to form a reversible intermediate product $Zn_3(OH)_2V_2O_7 \cdot 2H_2O$, which gradually decreases and disappeared during the charging process. Meanwhile, it can be observed that the diffraction peaks at 8.068° for $Zn_4SO_4(OH)_6 \cdot 5H_2O$ appears and increases gradually during the discharging process, which has been reported as an intermediate by-product during the aqueous ZIBs charging and discharging process [31].

The transposition of the KNiVO structure can also be certificated in SEM morphologies. As shown in Fig. S17a (Supporting information), the morphology of KNiVO is a major bulk crystal before activation. Then, the original structure became porous and plenty of micron-sized particles pile up together due to the displacement of Zn^{2+} to K^+ after the activation (Fig. S17b in Supporting information). Subsequently, with a considerable of K ions leaving, the KNiVO structure was mainly formed by the layered ions channels and 3D nanosized NiV_3O_8 clusters, which were connected more inseparable and still stable after a long cycling (Fig. S17c in Supporting information). Furthermore, in order to gain more insight from the morphology and crystal structure of the KNiVO sample after the cycling, transmission electron microscopy (TEM) analysis was utilized.

Figs. 4a and b show TEM images of the KNiVO cathode material before/after activation, and the elemental mapping images demonstrate the activation mechanism of the KNiVO that the K atoms were replaced by Zn atoms irreversibly while the Ni and V atoms

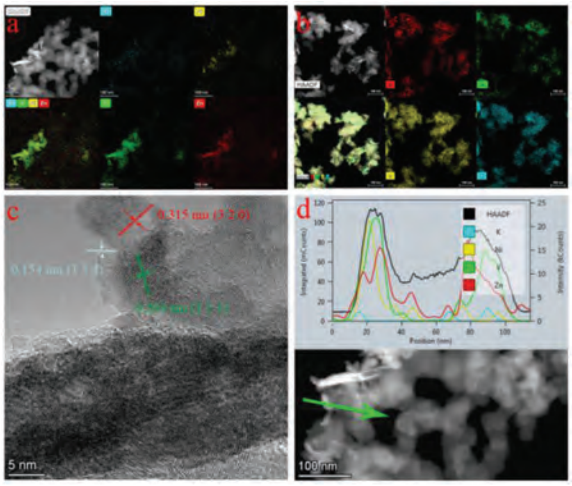

Fig. 4. (a, b) TEM images and the EDS elemental mapping of K, Ni, Zn and V before/after activation. (c) HRTEM images of activated KNiVO. (d) HAADF-STEM line scan and the data for K, Ni, V and Zn atoms.

were stable as an ion channels support. Fig. 4c shows the corresponding high-resolution TEM (HR-TEM) image of Fig. 4a. HR-TEM analysis shows that interplanar spacing of 0.154 and 0.315 nm corresponds to the (114) plane of $Zn_3(OH)_2V_2O_7{\cdot}2H_2O$ and the (320) plane of the NiV_3O_8, and the measured lattice spacing of 0.269 nm agrees well with the arrangement of KV_3O_8 in the (211) face. Besides, through the HAADF-STEM line scan data (Fig. 4d) we can more intuitively observe the content of K, Ni, V and Zn atoms, indicating that the content of Ni, V and Zn accounted for the majorities of the active material, while the content of K became very little after cycling. Therefore, both the SEM and TEM images testified that the activated KNiVO can act as a stable structure for Zn^{2+} transfer and storage channels, which also explain the activation mechanism and excellent performance of the Zn/KNiVO battery immediately. To prove the stable support role of NiV_3O_8 and the departure of K^+ during discharge/charge, the obtained cathode material was analysed by ICP-AES, and the results showed that the molar ratio of K:Ni:V was 1:1.5:7.5 before cycling (Table S1 in Supporting information). Moreover, the occurrence of K atoms in the ICP-AES results of electrolyte after discharge/charge process indicates a part of K^+ enter the electrolyte, while the Ni and V ions were not detected in the electrolyte (Table S2 in Supporting information). This result directly shows that the correlation of capacity stability and the NiV_3O_8 active material insoluble. For confirming the transformation process of the prepared material, Raman spectroscopic analysis was employed and the related results are portrayed in Figs. S18 and S19 (Supporting information). The Raman peaks located at 250–350 cm^{-1} are attributed to the Ni-O and the and the peaks located at 800–900 cm^{-1} are approximately the signature of the V-O, which strongly certificated the stability of NiV_3O_8. In addition, the Raman characteristic peaks for K-O were gradually disappeared at the low-frequency region from 50 cm^{-1} to 150 cm^{-1} after the cycling [58]. Moreover, Figs. S20 and S21 (Supporting information) display the V 2p XPS spectra of the electrodes at original and activated state. The fitted V $2p_{3/2}$ peak of the pristine KNiVO electrode at 517.3 eV and $2p_{1/2}$ peaks at 524.4 eV corresponds to V^{5+} species, after electrical activation another V $2p_{3/2}$ peak appears at 516.3 eV, which indicate partial reduction of V^{5+} to V^{3+} [13,54]. The XPS data illustrated that the departure of K^+ increased the redox activity of V^{5+}/V^{3+} after the activation. Therefore, it can speculate that the reaction mechanism of KNiVO as aqueous ZIBs cathode and the detailed electrode reactions are summarized in Fig. S22 (Supporting information). Firstly, in the activation process, Zn^{2+} ions insert into the KNiVO to produce KZnNiVO intermediate materials, with the further departure of K ions, the final structure is transformed into ZnNiVO. Then, V^{5+} showed redox activity due to the replacement of Zn^{2+} ions to K^+ ions, which began to participate in the cathodic redox. Afterwards, the $Zn_3(OH)_2V_2O_7{\cdot}2H_2O$ was generated as discharge products, which was partially oxidized during the charging process. Finally, a small amount of $Zn_3(OH)_2V_2O_7{\cdot}2H_2O$ was accumulated in the cathode, which can be observed after the cell through a long cycling (Fig. 5) [13].

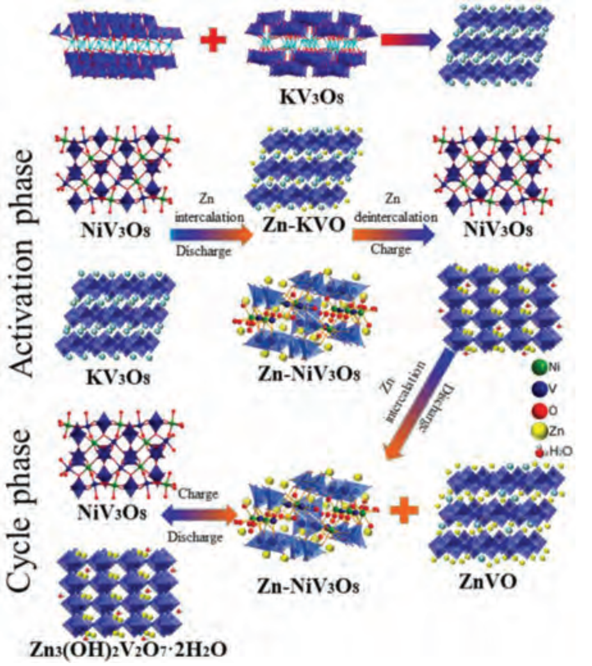

Fig. 5. The illustration of the Zn^{2+} in/deintercalation process in the cathode during the cycle phase.

In conclusion, a bi-component polyoxometalate-derivative cathode material was synthesized by using V_{10}-POM as the regulatory structural unit for the first time. This material is stable in the aqueous electrolyte, and the specific capacity can reach 229 mAh/g at a current density of 4 A/g, and the capacity is still at a high level after 4500 cycles. The electrochemical properties of vanadium-based oxides were significantly improved by this structural unit of binary blends. Layered KVO constitutes Zn^{2+} migration and storage channels, and K^+ was gradually replaced by Zn^{2+} in the activated phase. Besides, the NiVO clusters act as a steady supporting for ion channels. This bifunctional metal oxide material with definite mechanism provides a new research trend for the application of POMs and its ramification in energy storage.

Declaration of competing interest

The authors declare that they have no known competing financial interests or personal relationships that could have appeared to influence the work reported in this paper.

Acknowledgments

This work was supported by the Natural Science Foundation of Hunan Province (No. 2020JJ4684), the Fundamental Research Funds for the Central Universities of Central South University (No. 2021zzts0522) and the Recruitment Program of Global Youth Experts.

Supplementary materials

Supplementary material associated with this article can be found, in the online version, at doi:10.1016/j.cclet.2021.11.094.

References

[1] M.S. Balogun, W. Qiu, Y. Luo, et al., Nano Res. 9 (2016) 2823–2851.
[2] B. Dunn, H. Kamath, J.M. Tarascon, Science 334 (2011) 928.
[3] H.F. Dai, B. Jiang, X.S. Hu, et al., Renew. Sustain. Energy Rev. 138 (2021) 110480.
[4] D. Kundu, B.D. Adams, V. Duffort, et al., Nat. Energy 1 (2016) 16119.
[5] M.C. Lin, M. Gong, B. Lu, et al., Nature 520 (2015) 324.
[6] C. Xu, B. Li, H. Du, et al., Angew. Chem. Int. Ed. 51 (2012) 933.
[7] M. Song, H. Tan, D. Chao, et al., Adv. Funct. Mater. 28 (2018) 1802564.
[8] D. Kundu, S.H. Vajargah, L. Wan, et al., Energy Environ. Sci. 11 (2018) 881–892.
[9] H. Li, L. Ma, C. Han, et al., Nano Energy 62 (2019) 550–587.
[10] Y. Zhang, A.B. Chen, J. Sun, J. Energy Chem. 54 (2021) 655–667.
[11] P. He, Y.L. Quan, X. Xu, et al., Small 13 (2017) 1702551.
[12] Y. Li, W. Yang, W. Yang, et al., J. Energy Chem. 60 (2021) 233–240.
[13] K. Yang, Y.Y. Hu, L.Y. Li, et al., Nano Energy 74 (2020) 104851.
[14] X.Y. Liu, J. Yi, K. Wu, et al., Nanotechnology 31 (2020) 122001.
[15] S. Wang, S.W. Lu, X. Yang, et al., J. Electroanal. Chem. 882 (2021) 115033.
[16] J. Mao, F.F. Wu, W.H. Shi, et al., Chin. J. Polym. Sci. 38 (2020) 514–521.
[17] Q. Li, T.Y. Wei, K.X. Ma, et al., ACS Appl. Mater. Interfaces 11 (2019) 20888–20894.
[18] S. Islam, M.H. Alfaruqi, D.Y. Putro, et al., J. Mater. Chem. A 7 (2019) 20335.
[19] P. He, G.B. Zhang, X.B. Liao, et al., Adv. Energy Mater. 8 (2018) 1702463.
[20] H.G. Qin, L.L. Chen, L.M. Wang, et al., Electrochim. Acta 306 (2019) 307–316.
[21] X.Y. Wang, L.W. Ma, J.C. Sun, ACS Appl. Mater. Interfaces 11 (2019) 41297–41303.
[22] X.Y. Chen, L.B. Wang, H. Li, et al., J. Energy Chem. 38 (2019) 20–25.
[23] N. Zhang, Jia M, Y. Dong, et al., Adv. Funct. Mater. 29 (2019) 1807331.
[24] J. Cui, X.Y. Liu, Y.H. Xie, et al., Mater. Today Energy 18 (2020) 100563.
[25] N. Zhang, Y. Dong, M. Jia, et al., ACS Energy Lett. 3 (2018) 1366–1372.
[26] H.Z. Zhang, Q.Y. Liu, J. Wang, et al., J. Mater. Chem. A 7 (2019) 22079.
[27] M.S. Zhang, W.X. Wu, J.W. Luo, et al., J. Mater. Chem. A 8 (2020) 11642.
[28] A.X. Huang, W.J. Zhou, A.R. Wang, et al., Appl. Surf. Sci. 545 (2021) 149041.
[29] J. Cui, Z.W. Guo, J. Yi, et al., ChemSusChem 13 (2020) 2160–2185.
[30] S.W. Li, Y.C. Liu, X.D. Zhao, et al., Adv. Mater. 33 (2021) 2007480.
[31] C.X. Xu, Y. Zhang, N.Q. Zhang, et al., Chem. Asian J. 15 (2020) 3696–3708.
[32] Y. Liu, X.M. Zhou, R. Liu, et al., ACS Appl. Mater. Interfaces 11 (2019) 19191–19199.
[33] S. Khamsanga, M.T. Nguyen, T. Yonezawa, et al., Int. J. Mol. Sci. 21 (2020) 4689.
[34] H.J. Kim, R.H. Kim, S.S. Lee, et al., ACS Appl. Mater. Interfaces 6 (2014) 11692–11697.
[35] Y.J. Li, L. Cui, P.F. Da, et al., Adv. Mater. 30 (2018) 1804653.
[36] D.L. Long, L. Cronin, Dalton Trans. 41 (2012) 9815.
[37] Y.C. Ji, L.J. Huang, J. Hu, et al., Energy Environ. Sci. 8 (2015) 776.
[38] W.P. Deng, Q.H. Zhang, Y. Wang, Dalton Trans. 41 (2012) 9817.
[39] H. Wang, N. Kawasaki, T. Yokoyama, et al., Dalton Trans. 41 (2012) 9863.
[40] W. Chio, D. Im, M.S. Park, et al., Electrochemistry 84 (2016) 882–886.
[41] R.N.N. Khan, N. Mahmood, C.L. Lv, et al., RSC Adv. 4 (2014) 7374.
[42] T. Wei, M. Zhang, P. Wu, et al., Nano Energy 34 (2017) 205–214.
[43] K. Sun, H.Q. Li, H.J. Ye, et al., ACS Appl. Mater. Interfaces 10 (2018) 18657–18664.
[44] Y.H. Ding, J. Peng, S.U. Khan, et al., Chem. Eur. J. 23 (2017) 10338–10343.
[45] X.C. Zhao, G.L. Niu, H.X. Yang, et al., CrystEngComm 22 (2020) 3588.
[46] N. Kawasaki, H. Wang, R. Nakanishi, et al., Angew. Chem. Int. Ed. 50 (2011) 3471–3474.
[47] Y.C. Ji, J. Hu, L.J. Huang, et al., Chem. Eur. J. 21 (2015) 6469–6474.
[48] J. Hu, H.L. Diao, W.J. Luo, et al., Chem. Eur. J. 23 (2017) 8729–8735.
[49] X.X. Li, F.C. Shen, J. Liu, et al., Chem. Commun. 53 (2017) 10054.
[50] L.B. Ni, G. Yang, C.Y. Sun, et al., Mater. Today Energy 6 (2017) 53–64.
[51] F. Wan, Y. Zhang, L.L. Zhang, et al., Angew. Chem. Int. Ed. 58 (2019) 7062–7067.
[52] W.G. Xiu, L. Hao, L. Jian, et al., Adv. Mater. 22 (2010) 4944.
[53] J. Zhou, L. Shan, Z. Wu, et al., Chem. Commun. 54 (2018) 4457–4460.
[54] T.Y. Wei, Q. Li, G.Z. Yang, et al., J. Mater. Chem. A 6 (2018) 20402.
[55] S. Huang, C. Meng, M. Xiao, et al., Nano Energy 61 (2019) 462–470.
[56] B.K. Lesel, J.S. Ko, B. Dunn, et al., ACS Nano 10 (2016) 7572–7581.
[57] J. Wang, J. Polleux, J. Lim, et al., J. Phys. Chem. C 111 (2007) 14925–14931.
[58] E. Ni, S. Uematsu, Z. Quan, et al., J. Nanopart Res. 15 (2013) 1732.